ARTICLE

High-Corrosion-Resistance Mechanism of Graphitized Platelet-type Carbon Nanofibers under OER in Concentrated Alkaline Electrolyte

Received 00th January 20xx,
Accepted 00th January 20xx

DOI: 10.1039/x0xx00000x

Yuki Sato[a], Naohito Yamada[a], Sho Kitano[b]*, Damian Kowalski[b, c], Yoshitaka Aoki[b], Hiroki Habazaki[b]

Carbon materials are used as electrocatalyst supports and conductive additives in various electrodes for electrochemical energy conversion and storage because of their high electrical conductivity and chemical stability. However, they suffer from electrochemical corrosion at high anodic potentials in aqueous electrolytes. This study demonstrates that highly graphitized platelet-type carbon nanofibers (pCNFs) are tolerant to electrochemical corrosion under oxygen evolution reaction (OER) conditions in a concentrated KOH electrolyte. An identical-location scanning electron microscopy study showed that the corrosion rate of the carbon edge plane of the pCNFs is very low compared with that of the carbon basal plane. Further scanning transmission electron microscopy/electron-energy loss spectroscopy studies indicate that the carbon edge plane of the pCNFs is covered with hydroxyl groups, whereas the oxygen-containing species are limited to the carbon basal plane. Thus, most surfaces of highly graphitized pCNFs, consisting of the carbon edge plane, are passivated with hydroxyl groups, resulting in the high resistance of pCNFs to electrochemical corrosion. These findings provide a novel material design for carbon with a high corrosion resistance under the OER.

Introduction

Carbon is one of the key components in electrochemical energy conversion and storage systems, such as lithium-ion batteries,[1-6] electrochemical capacitors,[7-15] polymer electrolyte fuel cells (PEMFCs),[16-23] and metal-air secondary batteries (MABs).[24-31] However, carbon materials suffer from electrochemical oxidation; that is, carbon corrosion occurs in aqueous electrolytes at high anodic potentials, where many important electrochemical reactions, including the oxygen evolution reaction (OER), transpire. The thermodynamic instability of carbon is evident from the low equilibrium potential of carbon oxidation to CO_2 at 0.207 V vs. SHE at 25 °C.[32] The carbon oxidation reaction (COR) in alkaline electrolytes proceed through two elementary steps via the following reactions:[24, 32-38]

$$C + 4OH^- \rightarrow CO_2 + 2H_2O + 4e^- \quad (1)$$

$$CO_2 + 2OH^- \rightarrow CO_3^{2-} + H_2O \quad (2)$$

Alternatively, it occurs by a one-step reaction to yield carbonate at a standard electrode potential of -0.682 V vs. a Hg/HgO reference electrode (0.242 V vs. RHE at pH 14) at 25 °C in a 0.1 mol dm^{-3} CO_3^{2-} solution.[33]

$$C + 6OH^- \rightarrow CO_3^{2-} + 3H_2O + 4e^- \quad (3)$$

The COR induces electrode degradation because of the loss or agglomeration of electroactive species on carbon or the loss of electro-conductive paths when using carbon materials as the electrocatalyst support or conductive additive.[16-19, 23-31] When OER electrodes with noble-metal-free electrocatalysts were fabricated, carbon material was often added as conductive support because of the insufficient electric conductivity of electrocatalysts.[29-31] For developing the durable OER electrodes, the COR of the carbon conductive support must be avoided. Carbon materials have advantages compared to other conductive materials from the following points: i) earth-abundance, ii) lightweight, iii) reasonable electric conductivity, and iv) oxygen reduction reaction co-catalysis activity, which is the crucial characteristic of the air electrode in the metal-air secondary battery system. Because of such scientific background, tolerance to carbon corrosion is a prerequisite for the fabrication of durable carbon-containing electrodes.

Fujigaya *et al.* attempted to separate carbon materials from a corrosion environment by utilizing a polymer coating.[39-41] Increasing the graphitization degree and using low-defect structures of carbon materials are widely accepted approaches to suppress carbon corrosion.[42-46] For example, Ross *et al.* demonstrated that highly graphitized carbon obtained by heat treatment at 2700 °C has a lower corrosion rate than carbon with a low graphitization degree in a 30% KOH electrolyte at 55 °C.[42] Hung *et al.* investigated the corrosion behavior of carbon materials with different graphitization degrees using electrochemical quartz crystal microbalance and revealed improved tolerance to carbon corrosion with an increased degree of graphitization.[43]

[a] *Graduate School of Chemical Sciences and Engineering, Hokkaido University, Sapporo, Hokkaido 060-8628, Japan*
[b] *Division of Applied Chemistry, Faculty of Engineering, Hokkaido University, Sapporo, Hokkaido 060-8628, Japan*
[c] *Biological and Chemical Research Centre (CNBCh), Faculty of Chemistry, University of Warsaw, ul. Żwirki i Wigury 101, 02-089, Warsaw, Poland*
Electronic Supplementary Information (ESI) available: [details of any supplementary information available should be included here]. See DOI: 10.1039/x0xx00000x

Graphitic carbon has a stacked-layer structure with the surface consisting of either a carbon edge plane or a basal plane. The carbon edge plane is significantly more reactive than the basal plane;[47] thus, it is believed to be the preferred oxidation site.[48-51] However, some opposing experimental results were reported recently for platelet-type carbon nanofibers (pCNFs). The pCNFs possess a structure with graphene layers arranged perpendicularly to the fiber axis of the nanofibers. Further, the sidewall of the nanofibers consists of the carbon edge plane, whereas the carbon basal plane is exposed at the end of the pCNFs.[52, 53] This suggests that the surface of pCNFs is mainly composed of the edge plane. Therefore, a higher corrosion rate is expected for the pCNFs than for other nanostructured carbon materials; however, the results contradict this.[18, 29, 54, 55] Tamaki *et al.* compared the durability of Pt/carbon black and Pt/pCNF under PEMFC operation conditions.[54] Pt/pCNF exhibited greater durability despite showing a lower graphitization degree, as estimated from the Raman spectra. Tsuji *et al.* also reported the improved durability of Pt/pCNFs, which increased with the enhanced graphitization degree of the pCNFs.[18] Lee *et al.* demonstrated the enhanced durability of Pt/pCNF and hybrid-type Pt/(pCNF + activated carbon) compared with that of Pt/activated carbon under an accelerated durability test using a PEMFC cathode.[55]

Recently, our group examined the stability of pCNFs under the OER, a charging reaction of MABs, in a concentrated alkaline electrolyte and compared it with that of other carbon materials.[29] Interestingly, pCNF showed long-term durability of more than one month, despite other carbon materials, including carbon black and multi-walled carbon nanotubes, corroding within two weeks. These recent findings suggest the possible high tolerance to oxidation of the carbon edge plane of pCNFs at high potentials in alkaline electrolytes, as opposed to the generally accepted high reactivity of the carbon edge plane. In this study, the corrosion rate of highly graphitized pCNFs and carbon blacks at a high anodic potential in a 4 mol dm^{-3} KOH electrolyte was quantitatively analyzed using an identical-location scanning electron microscopy (ILSEM) technique. The corroded carbon edge and basal planes were further examined by scanning transmission electron microscopy (STEM)/electron-energy loss spectroscopy (EELS) analysis to gain insights into the mechanism of the improved corrosion resistance of pCNFs.

Results and Discussion

Material characterizations

The carbon materials used in this study were as follows: pCNFs heat-treated at 2000 (pCNF2000), 2400 (pCNF2400), and 3000 °C (pCNF3000), and two types of commercial carbon blacks (TB: Tokai Carbon, TOKA Black#3800 and AB: Strem Chemicals, acetylene black). **Fig. 1** shows the SEM and TEM images of the carbon materials used in this study and the schematic illustrations of carbon materials. AB (Fig. 1a) and TB (Fig. 1c) revealed nanoparticle-type morphologies with diameters of 50–150 nm. The TEM image of TB (Fig. 1d) revealed well-developed lattice fringes, corresponding to the (002) lattice plane, whereas AB (Fig. 1b) showed less-developed lattice fringes, indicating a lower degree of graphitization.

The lattice fringes are almost parallel to the carbon black surfaces; that is, the basal plane of carbon is exposed to the surface.

Fig. 1e, 1g, and 1i shows the nanorod-like morphology of the pCNFs. For pCNF2000 and pCNF2400, prepared by liquid-phase carbonization using a porous anodic alumina template,[2, 7, 18, 21, 29, 52] the diameters, controlled by the template pore size, were ~55 nm. In contrast, the fiber diameter of pCNF3000, prepared by a catalytic chemical vapor deposition method, varied between 80 and 300 nm. The TEM images of all the pCNFs exhibited the platelet structure of the carbon nanofibers; that is, the carbon layers were normal to the fiber axis. An additional interesting feature is the looped structure that developed at the edges of the carbon layers. The loops developed during heat treatment at high temperatures ≥ 2000 °C (Fig. 1l), possibly reducing the high surface energy of dangling bonds at the sidewalls of the pCNFs.[56]

The X-ray diffraction (XRD) patterns of the carbon materials shown in **Fig. 2a** reveal a strong peak at approximately $2\theta = 26°$ and a relatively weak diffraction peak at approximately $2\theta = 42°$, corresponding to the 002 and 10 reflections of graphitic carbon, respectively. In addition to the reflections corresponding to AB, a very weak 004 reflection appeared at approximately 52°. The carbon 002 reflection peak intensified and sharpened upon increasing the heat treatment temperature of the pCNFs, which is associated with an increased graphitization degree. The 002 lattice spacing, d_{002}, of the carbon materials used in this study was measured and is summarized in **Table 1.** The d_{002} values of the pCNFs heat-treated at wider temperatures,[52] multi-walled carbon nanotubes (MW),[29] and other carbon black materials[29] are also summarized in **Table S1**. The d_{002} values of the pCNFs decreased with increasing heat treatment temperature and approached the value for graphite (0.3354 nm). The d_{002} value of TB was between those of pCNF2000 and pCNF2400, and AB exhibited the highest d_{002} value, which indicates the lowest degree of graphitization.

Table 1. Physicochemical properties of the carbon materials used in this study

	Lattice spacing, d_{002} / nm	I_D/I_G	BET surface Area / $m^2\ g^{-1}$
pCNF2000	0.343	1.71	27.0
pCNF2400	0.340	1.51	28.0
pCNF3000	0.336	0.725	40.3
TB	0.342	0.392	26.4
AB	0.352	1.04	78.0

Raman spectroscopy was also used to investigate the degree of graphitization of the carbon materials. As shown in Fig. 2b, the Raman spectra reveal two peaks at ~1350 and ~1580 cm^{-1}, which are associated with the A_{1g} (D band) and E_{2g} vibration (G band), respectively. In addition, a weak shoulder peak of the D' band appeared at ~1620 cm^{-1}. The peak area ratios of I_D/I_G, which are often used to evaluate the graphitization degree of carbon materials,[54] are summarized in Table 1. The peak width

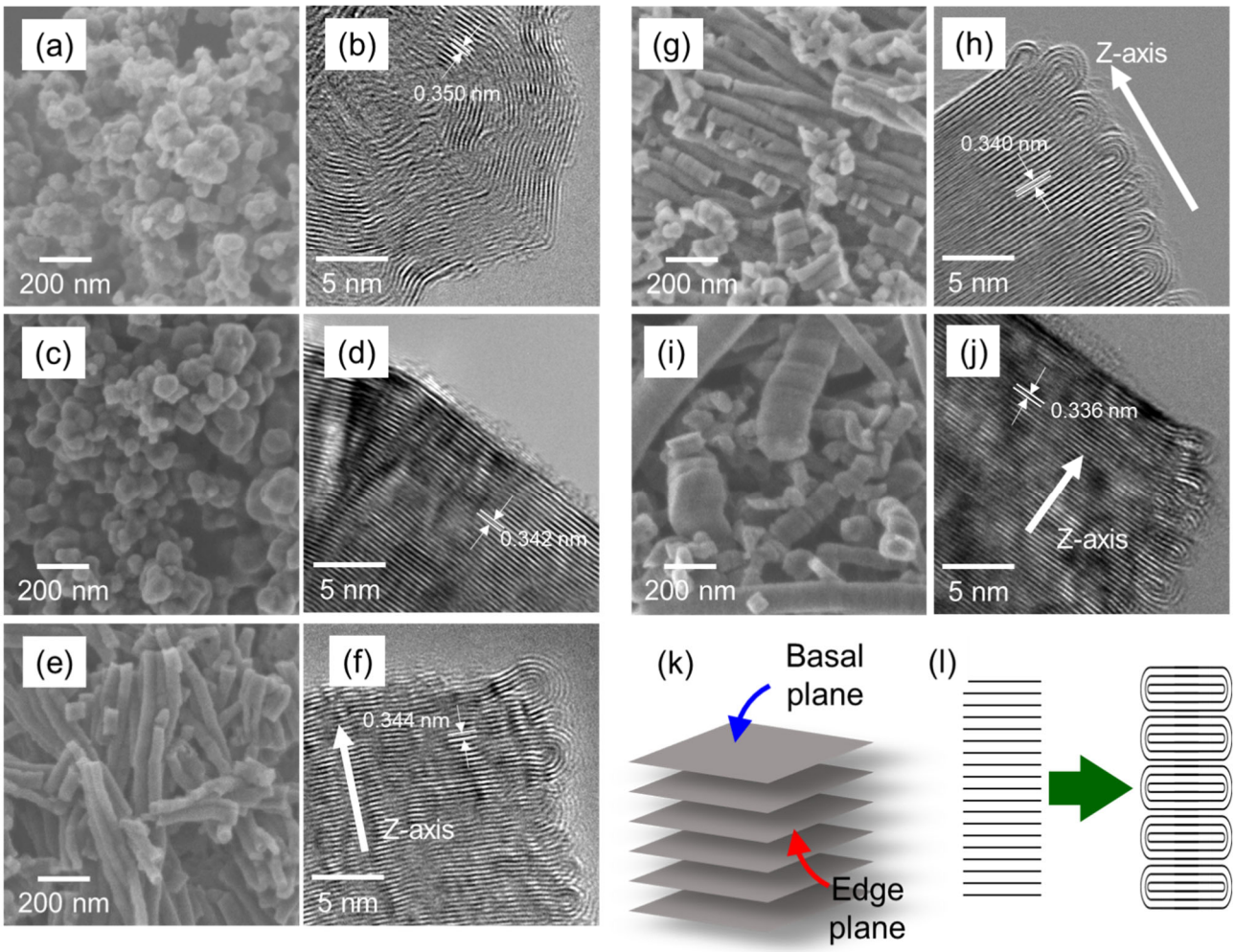

Fig. 1 SEM and TEM images of the carbon materials used in this study: (a–b) AB, (c–d) TB, (e–f) pCNF2000, (g–h) pCNF2400, and (i–j) pCNF3000. Schematic illustrations of (k) the crystalline structure of the carbon material and (l) the loops formation.

of the G band is another parameter used to evaluate the degree of graphitization.[54] The correlations between I_D/I_G and d_{002} and between the peak width of the G band and d_{002} are plotted in Fig. 2c and 2d, respectively. The results of MW and Denka black, examined in our previous study,[29] are also added in these figures. There is a good correlation between the I_D/I_G value and d_{002} for the pCNFs, but this linear correlation is different from other carbon materials. In contrast, all the carbon materials exhibited a linear correlation between the width of the G band and d_{002}. A relatively higher I_D/I_G value of pCNFs compared to other carbon materials is possibly related to the platelet structure providing many edge sites; [54] the I_D/I_G value of pCNFs is influenced significantly by the presence of the looped carbon layers with many disordered carbons at their sidewall. In contrast, the G band's peak width mainly reflects the structure of the bulk region of carbon materials. Thus, the I_D/I_G value – d_{002} correlation can be used to estimate the disorder degree of sidewall region of pCNFs, whereas the peak width of the G band and d_{002} can be applied to evaluate the graphitization degree of the bulk region of diverse carbon materials.

The nitrogen gas adsorption/desorption isotherms for the carbon materials used in this study are shown in **Fig. S1**. All isotherms show an IUPAC type III curve, suggesting a limited number of micro- and mesopores. The Brunauer–Emmett–Teller (BET) surface areas, estimated from the adsorption isotherms, are summarized in Table 1. pCNF2000 and pCNF2400 have similar BET surface areas because of the template-based preparation of these two pCNFs. TB also exhibits a similar BET surface area, whereas pCNF3000 and AB possess greater BET surface areas. However, all the carbon materials show BET surface areas of 25–80 $m^2\ g^{-1}$, which is typical for conductive carbon additives used for electrode applications.

ILSEM study

The corrosion rates of the carbon materials at 1.8 V vs RHE in a 4.0 mol dm^{-3} KOH electrolyte were examined using the ILSEM technique (**Fig. S2**).[57-61] The size reduction of each nanoparticle and nanofiber by carbon corrosion was measured by comparing the SEM images before and after polarization. The carbon nanoparticles and nanofibers were deposited on a surface-roughened Au TEM grid (Fig. S2c) with a Nafion binder, and nanoparticles and nanofibers at identical locations were observed after polarization under the OER. Au is stable under the OER in alkaline electrolytes.[62] The surface roughening of the Au grid by the anodizing method[63-65] effectively reduced carbon nanoparticle and nanofiber detachment during polarization owing to the anchoring effect.[66-68]

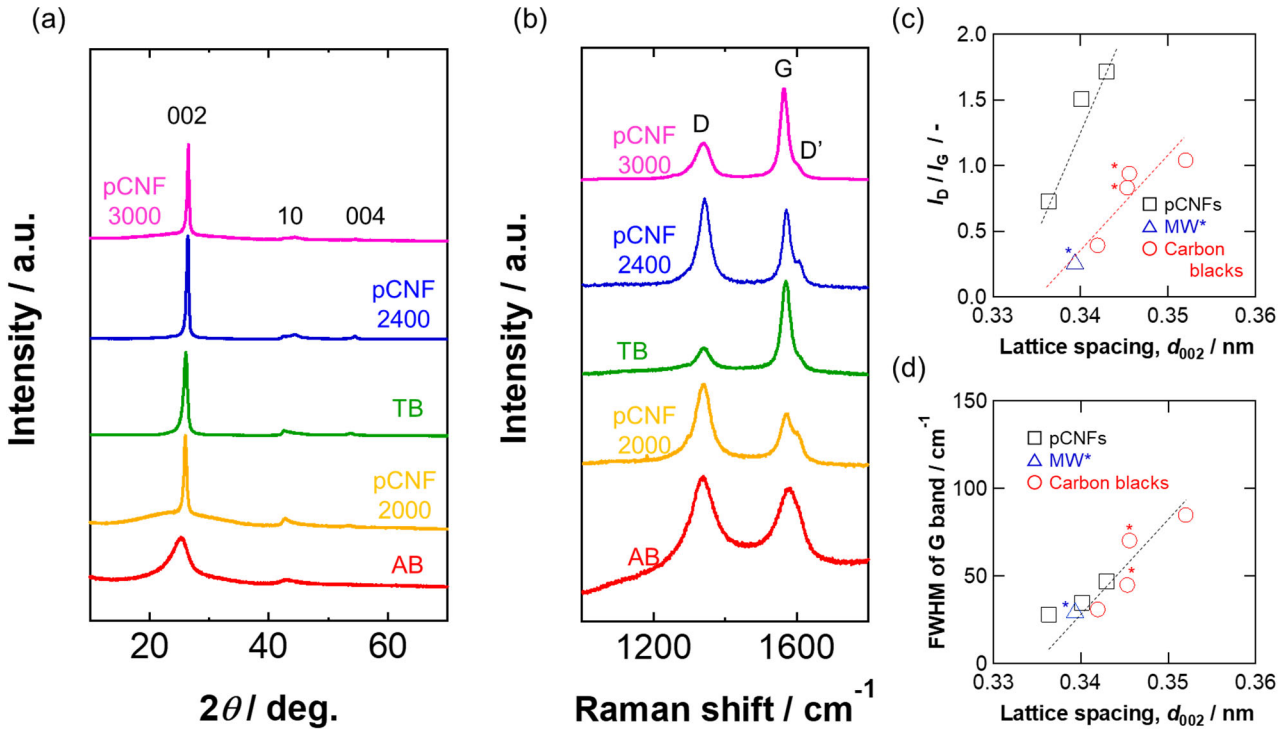

Fig. 2 (a) XRD patterns and (b) Raman spectra of the carbon materials used in this study; (c, d) the relationship between the lattice spacing and I_D/I_G calculated from Fig. 2b, and the FWHM of the G band that appeared in Fig. 2b. In Fig. 2c and d, ○* depicts the data of Denka black carbon obtained in our previous work.[29] △* also depicts the data of MW obtained in our previous work.[29]

Examples of the ILSEM study of TB and AB nanoparticles are shown in **Fig. 3** and **Fig. S3**, respectively. The TB particle size decreased with the polarization time without significant changes in the shape of the particles, suggesting the uniform oxidation of TB nanoparticles. The diameter reduction was measured for more than 10 nanoparticles and plotted as a function of polarization time (Fig. 3d). The diameter of TB decreased linearly with time at an average rate of 0.46 nm h^{-1}. A higher oxidation rate was found for the AB nanoparticles, which exhibited a lower graphitization degree than the TB nanoparticles. From Fig. S3, the diameter of AB decreased by 17.5 ± 7.6 nm after polarization for 24 h, corresponding to a diameter reduction rate of 0.73 nm h^{-1}. We conducted prolonged polarization for the AB nanoparticles but were unable to successfully measure the decreased diameter because of significant nanoparticle detachment.

Fig. 4 shows the ILSEM results for the pCNFs. The length of the pCNFs decreased during polarization at 1.8 V vs RHE. For pCNF2400, the fiber length decreased by 10.9 ± 6.4 and 20.2 ± 9.9 nm after 24 and 48 h polarization, respectively. Thus, assuming that the length reduces linearly with the polarization time, the length reduction rate was estimated to be 0.42 nm h^{-1}. This value decreased from 0.62 nm h^{-1} for pCNF2000 to 0.34 nm h^{-1} for pCNF3000 upon increasing the heat treatment temperature of pCNFs. The carbon oxidation rate of the carbon blacks and pCNFs was estimated from the diameter and length reduction rates and plotted as a function of d_{002} (Fig. 4k). An approximately linear relationship was observed, indicating that the degree of graphitization controls carbon oxidation, as reported previously.[42-46] The outer surface of the carbon blacks and the end surface of the nanofibers consisted of the carbon basal plane. The results in Fig. 4k indicate that the oxidation resistance of the carbon basal plane improves with increasing graphitization degree.

The most striking results were found for the carbon oxidation rate of the sidewall of the pCNFs. Assuming a similar corrosion rate to that of the basal plane of pCNF2400, we estimated the nanofiber diameter to be approximately half that after polarization for 48 h. However, the actual change in the nanofiber diameter for all the pCNFs was negligible, especially between 24 and 48 h (Fig. 4a–4i). The significantly reduced oxidation rate of the sidewall is observed in Fig. 4j; therefore, the sidewall of the pCNFs, comprising the carbon edge plane, is much more resistant than the highly graphitized carbon basal plane. The diameter of pCNF2000 and pCNF2400 decreased by 5 nm within the first 24 h and decreased to 2 nm or less during the subsequent 24 h. The slightly higher oxidation rate within the initial 24 h is discussed later. Assuming the pCNF of 50 nm diameter the length of 1 μm, the basal plane area ratio to the total surface area is only 2.5%. Thus, the overall corrosion rate of the pCNFs with a high aspect ratio is mainly controlled by their sidewall.

The chronoamperometry curves during the anodic polarization is shown in **Fig. S4**. The corrosion current of carbon materials, estimated from their size reduction, is negligible compared with the anodic currents observed in Fig. S4. Thus, the OER is a predominant anodic reaction, and the pCNFs exhibit a higher OER current than the carbon blacks, because of the higher OER activity of the carbon edge plane.

TEM observation

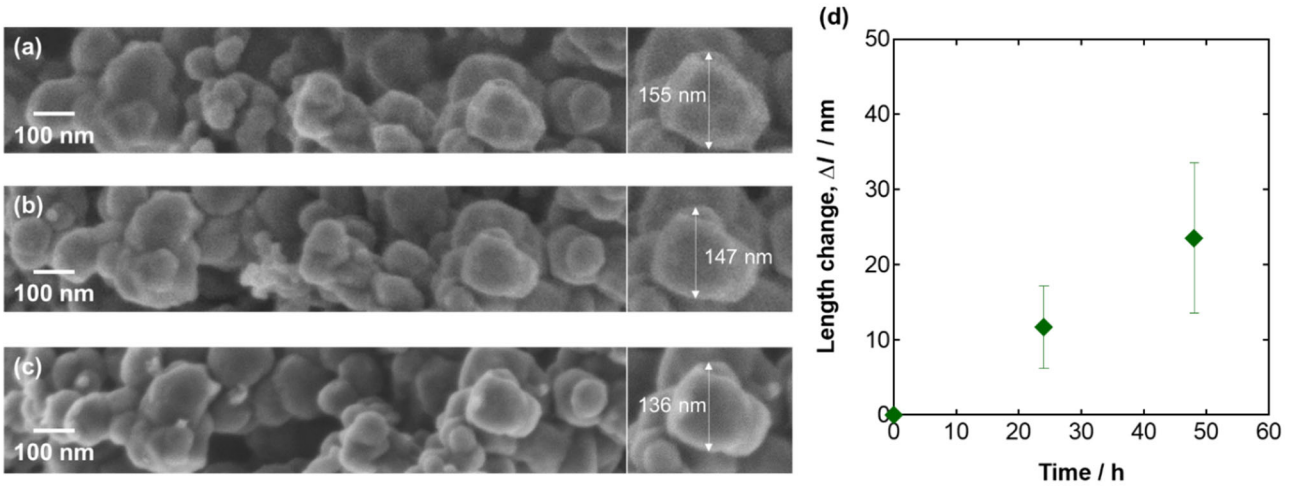

Fig. 3 (a-c) Identical-location SEM observation images of the TB loaded electrode (a) before and (b) after polarization at 1.8 V vs RHE for 24 h and (c) for 48 h. (d) The relationship between the change in diameter and the duration time calculated from Fig. 3 (a-c).

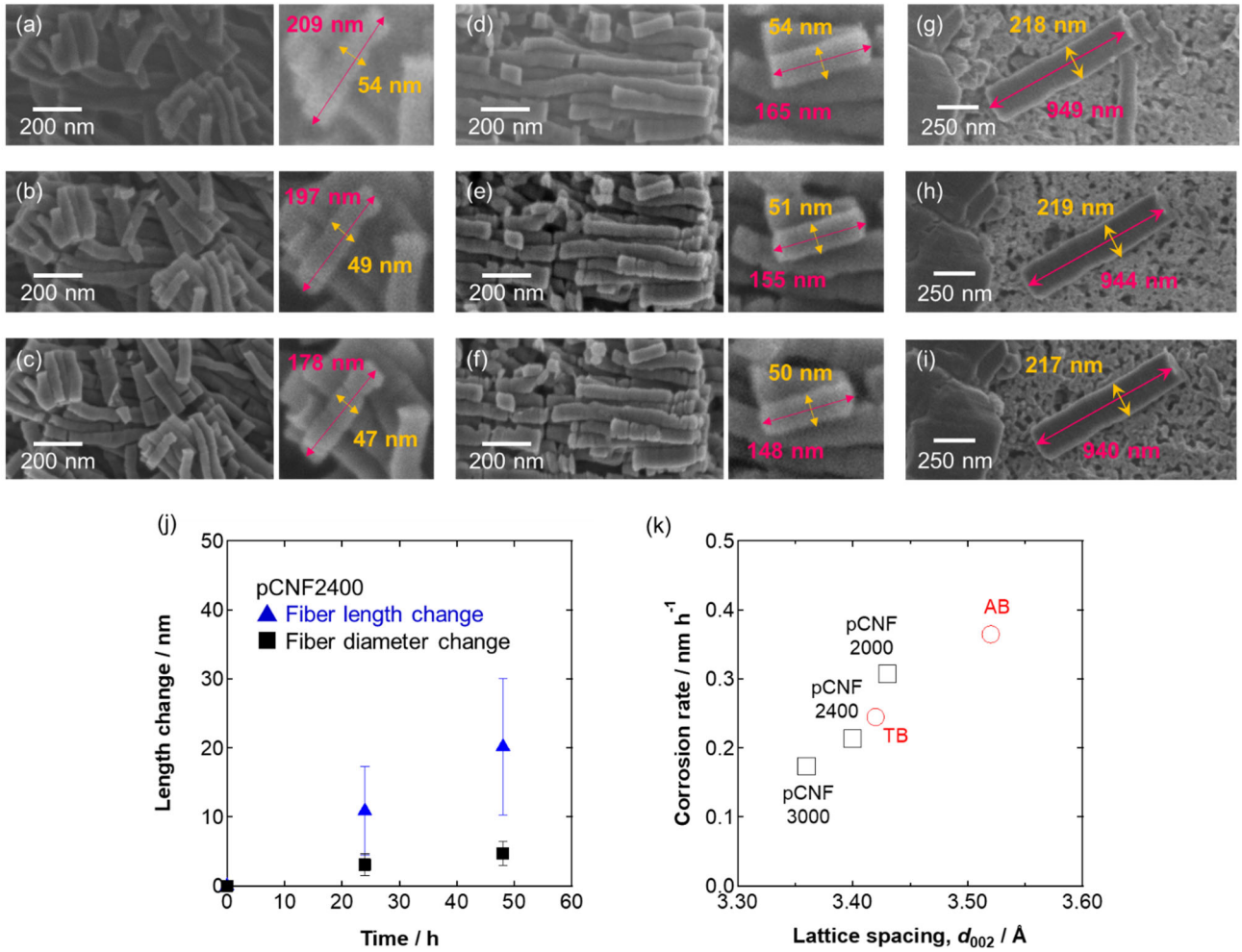

Fig. 4 Identical-location SEM observation images of pCNF loaded electrodes for (a–c) pCNF2000, (d–f) pCNF2400, and (g–i) pCNF3000. Each electrode was observed (a, d, g) before and (b, e, h) after polarization at 1.8 V vs RHE for 24 h and (c, f, i) 48 h. (j) The relationship between the change in the diameter and length of pCNF2400 and the duration time calculated from Fig. 4 (d-f). (k) The relationship between the lattice spacing of d_{002} and the basal plane corrosion rates.

The change in the carbon structure due to corrosion was further examined by TEM. **Fig. S5** shows the TEM images of AB before and after polarization for 24 and 48 h. The 002 lattice fringes observed in the pristine AB became obscure after polarization, suggesting a decrease in the graphitization degree. In addition, some particles were hollow after polarization, suggesting the preferential oxidation of carbon in the inner core regions. The inner core regions of pristine AB appeared to possess a lower graphitization degree, which increased the corrosion-induced loss of carbon. A similar morphological change was observed for

TB (**Fig. S6**). In contrast to AB, the 002 lattice fringes of TB remained unchanged even after polarization for 48 h; thus, the oxidation of TB proceeds without degradation of the high graphitization degree. The thickness of the well-developed graphitic layers from the outer surface was 14.3 ± 5.5 nm in the pristine TB, which reduced to ~7.2 and ~4.3 nm after polarization for 24 and 48 h, respectively. The oxidative removal of TB appears to proceed by uniformly consuming the graphene layer from the outer surface.

Changes in the carbon edge plane were examined by exposing the pCNFs to the electrolyte at a high potential, as shown in **Fig. 5** for pCNF2400. The TEM images of pCNF2000 and pCNF3000 are shown in **Fig. S7** and **S8**, respectively. In all the pCNFs, the loops that developed at the sidewall of the nanofibers disappeared, and the carbon edge plane was directly exposed to the electrolyte after polarization for 24 and 48 h.

The thickness of the looped carbon layer was ~2 nm; therefore, the oxidative removal of the loops decreased the diameter of pCNFs by ~4 nm, corresponding to the actual diameter reduction that occurred within 24 h (Fig. 4). Thus, the diameter reduction of the pCNFs within 24 h is mainly due to the oxidation of looped carbon, and the carbon corrosion becomes negligible after the exposure of the carbon edge plane to the electrolyte. The carbon corrosion rates at the sidewall of the pCNFs were almost independent of the heat treatment temperature, despite the reduced corrosion rate of the carbon basal plane with increasing graphitization degree (Fig. 4k). Although the degree of graphitization influenced the corrosion of the basal plane, it had a less significant effect on the edge plane.

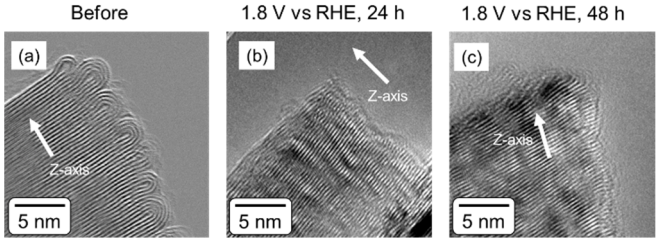

Fig. 5 TEM images of pCNF2400 (a) before and (b, c) after the polarization at 1.8 V vs RHE in 4.0 mol dm^{-3} KOH aq. for (b) 24 h and (c) 48 h.

STEM/EELS study

STEM combined with EELS is suitable for analyzing the local structure and chemistry at the nanometer and sub-nanometer scales. **Fig. 6** shows the STEM images of TB and pCNF2400 after 24 h anodic polarization at 1.8 V vs RHE and the low-loss EELS spectra of the numbered regions in Fig. 6a and 6b. In the low-loss region of the carbon materials, a broad peak appears between 10–40 eV and is identified as a combination of π and σ electronic excitations.[69-72] The spectra of the bulk region for TB and pCNF2400 show a π + σ peak at 26 eV, which is assigned to graphite. In addition, each carbon surface showed an additional π + σ broad peak at approximately 16 eV. Mkhoyan *et al.* reported that this peak is observed when sp^3-type carbon or oxygen is incorporated into graphitic carbon, that is, amorphous carbon or graphene oxide.[69] Therefore, the peak at 16.0 eV probably indicates the incorporation of oxygen species on the surface after anodic polarization. The intensity of the 16 eV peak is higher than that of the 25.9 eV peak at the pCNF edg plane surface, whereas the opposite is observed on the basal plane surface (TB surface and pCNF basal), reflecting the higher degree of oxygen incorporation on the edge plane surface than

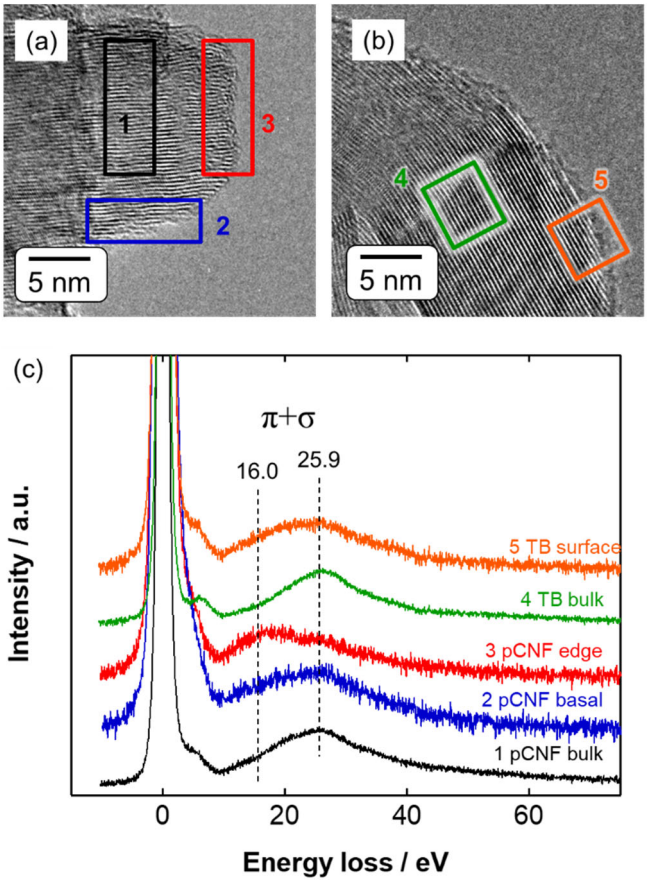

Fig. 6 STEM/EELS area analysis results for pCNF2400 and TB after the polarization at 1.8 V vs RHE in 4.0 mol dm^{-3} KOH aq. for 24 h. (a, b) STEM image of pCNF2400 (a) and TB (b). The analysis area is shown as the colored box. (c) EEL spectra around low-energy loss electrons for each analysis area.

that on the basal plane surface; that is, there is greater oxygen enrichment on the edge plane surface.

Fig. 7 shows the carbon K-edge EELS spectra of pCNF2400 and TB after 24 h of anodic polarization. The size of the analyzed points was less than 1 nm, and the surface regions of the carbon edge plane, basal plane, and inner regions of pCNF2400 and TB were analyzed. All spectra show a peak at 285.5 eV, corresponding to the π* electronic transition of the sp^2 type carbon.[70-74] Only the edge surface spectra of TB and pCNF2400 showed a shoulder at the higher-energy region of 286 eV. This region is assigned to the C–OH bonds of hydroxyl groups (**Table S2**).[70-74] Therefore, the EELS results revealed the introduction of hydroxyl groups on the edge plane surface after anodic polarization at 1.8 V vs RHE. As mentioned above, the ILSEM and TEM observations demonstrate that the carbon corrosion on the carbon edge plane is negligibly slow compared with that on

the carbon basal plane. The surface hydroxyl groups that developed on the edge plane of the pCNFs may be responsible for the significantly reduced corrosion rate. The presence of hydroxyl groups on the surface of the pCNFs was supported by contact angle measurements of a water droplet (**Fig. S9**). The water contact angle of the pristine pCNF2400 was 109.8 ± 2.3°, which reduced significantly to 28.5 ± 8.0° after anodic polarization at 1.8 V vs RHE for 2 h. In contrast, the water contact angle on the TB, which consisted mainly of the carbon basal plane, decreased to 79.6 ± 7.7°.

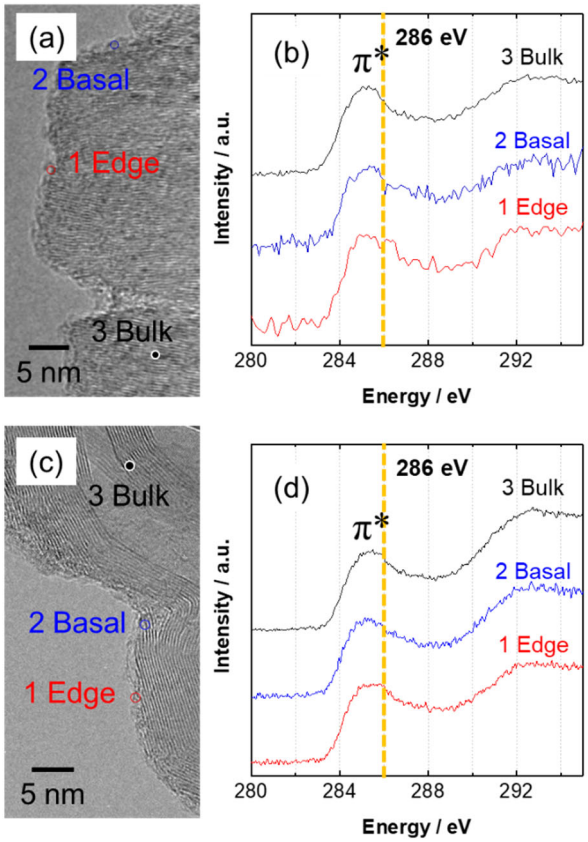

Fig. 7 STEM/EELS point analysis (ϕ < 1 nm) results for pCNF2400 and TB after the polarization at 1.8 V vs RHE in 4.0 mol dm^{-3} KOH aq. for 24 h. (a, c) STEM image of (a) pCNF2400 and (c) TB. (b, d) C-K edge of core-loss EEL spectra for each analysis points of (b) pCNF2400 and (d) TB.

Mechanism of high resistance toward carbon corrosion

The ILSEM results indicate that the carbon oxidation proceeds almost linearly with time on the carbon basal plane of carbon blacks and pCNFs at 1.8 V vs RHE in a 4 mol dm^{-3} KOH electrolyte (Fig. 3 and 4). The carbon oxidation rate on the basal plane decreased as the graphitization degree of the carbon materials increased. Additional structural disorder is present in the carbon materials with lower graphitization degrees. The disordered carbon atoms may be preferential carbon corrosion sites, which suggests that the carbon materials with lower disorder exhibit lower carbon oxidation rates on the basal plane. In contrast, the carbon oxidation of the edge plane of the pCNFs was extremely slow, regardless of the graphitization degree (Fig. 4). The carbon loops present in the pristine pCNFs disappeared after 24 h of anodic polarization. The looped carbon may corrode at a rate similar to that of the carbon basal plane, but the corrosion rate decreases significantly after exposure of the carbon edges. As shown in Fig. 1f, the platelet structure developed at a heat treatment temperature of 2000 °C, although the disorder appears to be present in the TEM image. These findings suggest that the carbon oxidation on the edge plane is not influenced by the graphitization degree or disordered structure when the carbon edge plane is uniformly exposed to the alkaline electrolyte. Instead, a passive surface developed on the carbon edge plane to suppress carbon corrosion such that it became negligible. Notably, the pCNF2400 mixed with the Ca_2FeCoO_5 electrocatalyst did not show noticeable fiber diameter reduction even after anodic polarization at a constant current density of 40 mA cm^{-2} for 1 month.[29] Such long-term durability of pCNF2400 may be due to the passivation of the carbon edge plane.

The passivation of the carbon edge plane of pCNFs occurs due to hydroxyl species. The STEM/EELS results indicated that the carbon edge plane of pCNFs is covered with hydroxyl species, which passivated the surface to electrochemical corrosion. Rather low water contact angle of the pCNF2400 after anodic polarization for 2 h supported the presence of hydroxyl species on the surface. Han *et al.* conducted the density functional theory (DFT) calculations of the stability of edge-oxygenated groups on graphene nanoplatelets.[50] The calculations indicated the energetic stability of the hydroxyl group at the graphene edge site, although they reported the highest stability of the in-plane etheric rings at the graphene edge site theoretically and experimentally in sulfuric acid. They concluded that the in-plane etheric rings at the graphene edge exhibited the best stability against anodic corrosion and chemical oxidation by H_2O_2. However, the present study demonstrated the formation of hydroxyl species on the carbon edge plane of pCNFs. Such different results may come from the different experimental conditions, including acid and alkaline environments and potential regions and the difference of carbon materials (pCNFs with stacked carbon layers and graphene).

Lin *et al.* examined the explicit roles of heteroatom-free carbon edge sites on ORR from the DFT calculations. [75] They reported that hydroxyl-adsorbed zigzag carbon edges become active sites for the OER with high stability. During the OER, the hydroxyl species are converted to C-O and C-OOH intermediates, but no C-O bond cleavage occurs, which likely suppresses carbon corrosion. In fact, the OER activity of the present pCNFs was higher than that of carbon black materials, as shown in Fig. S9, in which the pCNFs passivated with hydroxyl species exhibited high anodic current compared to the two types of carbon blacks that exposed mainly the carbon basal plane.

The hydroxyl groups do not form on the carbon basal plane at a high density, which is evident from the low oxygen concentration in the STEM/EELS analysis and relatively high water contact angle of carbon blacks that expose mainly the carbon basal plane. Thus, sufficient passivation cannot occur, and the electrochemical corrosion of carbon proceeds continuously on the basal plane of the carbon blacks and pCNFs

under investigation. The effective passivation of the carbon edge plane to suppress carbon corrosion has not been reported because the carbon materials that expose the edge plane predominantly are not readily available. The surface of pCNFs used in this study is composed mainly of a carbon edge plane after removing looped carbon layers, demonstrating the effective passivation by hydroxyl groups for the first time. The highly graphitized pCNFs can be developed readily using CVD and post-high-temperature heat treatment, so that the graphitized pCNFs are promising corrosion-resistant carbon materials in electrochemical energy conversion systems.

The changes in the edge and basal planes of the pCNFs during anodic polarization are illustrated in **Fig. 8**. The sidewalls of the pCNFs were initially covered with looped carbon layers, which were readily oxidized during anodic polarization, and carbon edges were exposed. Then, the hydroxyl species covered the edge surface at a high density, causing passivation of the sidewall of the pCNFs. After anodic polarization at 1.8 V vs RHE for 2 h, the water contact angle of pCNF2400 was reduced to 28.5 ± 8.0°, which was significantly lower than 79.6 ± 7.7° for TB. This low water contact angle of pCNF2400 suggests the presence of a high density of hydroxyl species on the sidewall of the pCNFs. In contrast, the hydroxyl species coverage of the carbon basal plane at both ends of the pCNFs and carbon black surfaces was relatively low, resulting in insufficient passivation. Thus, the continuous oxidation of carbon to CO_2 and CO [37, 76, 77] proceeds on the basal plane with an oxidation rate dependent on the graphitization degree. The findings of this study revealed that the uniform exposure of the carbon edge plane to the alkaline electrolyte is of great importance for suppressing carbon corrosion at high anodic potentials.

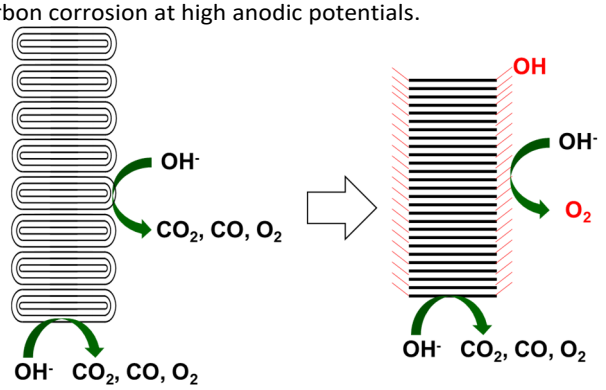

Fig. 8 Schematic illustration of the proposed corrosion mechanism of carbon materials under oxygen evolution reaction in 4.0 mol dm^{-3} KOH aq. at 1.8 V vs RHE.

It should be noted that the carbon edge plane was often reported to be preferential oxidation sites of graphitic carbon materials.[42, 48, 49] For instance, Matsumoto *et al.* conducted an electrochemical STM study of corrosion of highly oriented pyrolytic graphite (HOPG) in an acid electrolyte, and disclosed corrosion initiation at the step edge of HOPG, followed by fast oxidation along the in-plane direction.[49] They concluded the high resistance of the HOPG basal plane to corrosion. Staud *et al.* examined the corrosion of several carbon blacks heat-treated at 2700°C in 35% KOH electrolyte at 55°C.[42, 48] They reported the marked reduction of the corrosion rate when the graphitization degree was highly enhanced, but the preferential oxidation sites were reported to be the carbon edge plane. However, the current pCNFs with high graphitization degrees revealed the preferential passivation at the carbon edge plane. This may be a unique feature of pCNFs that expose the edge planes on the entire sidewall of pCNFs. The high surface coverage of carbon by hydroxyl species is likely to be a requisite for the effective passivation of carbon in a concentrated alkaline electrolyte.

Conclusions

In this study, pCNFs with high graphitization degrees were found to be highly resistant to carbon corrosion at high anodic potentials, at which the OER occurs, in a concentrated alkaline electrolyte. The corrosion rate on the carbon edge plane, determined quantitatively using the ILSEM technique, was negligible after the oxidative removal of the looped carbon layer on the carbon edge plane. The graphitization degree of pCNFs heat-treated at temperatures ≥ 2000 °C hardly influenced the carbon edge plane corrosion rate, whereas the basal plane corrosion rate decreased as the degree of graphitization increased. The high corrosion resistance of the pCNFs is attributed to the passivation of the carbon edge plane by covering it with a high density of hydroxyl species. The hydroxyl species could not sufficiently cover the carbon basal plane, resulting in the continuous oxidation of carbon on the basal plane. Thus, most surfaces of highly graphitized pCNFs, except the limited area of both ends of nanofibers, can be passivated by hydroxyl species, resulting in excellent corrosion resistance. Carbon materials are useful as supports for electrocatalytic nanoparticles, including Pt and transition metal oxide nanoparticles, and as conductive additives in alkaline fuel cells and aqueous metal-air rechargeable batteries. In such electrochemical energy conversion devices, corrosion-resistant carbon materials are required, and the current study demonstrates that highly graphitized pCNFs are promising for such applications. Thus, the uniform coverage of the carbon edge plane with hydroxyl species is key for passivation and provides an important path for the design of corrosion-resistant carbon materials.

Author Contributions

Y. Sato; Conceptualization, Investigation, Resources, Formal analysis, Data curation, Visualization, Writing- Original draft preparation, Funding acquisition, Methodology.: **N. Yamada**; Investigation.: **S. Kitano**; Supervision.: **D. Kowalski**; Visualization, Supervision, Investigation, Methodology.: **Y. Aoki**; Visualization, Supervision.: **H. Habazaki**; Conceptualization, Supervision, Visualization, Resources, Writing- Review & Editing, Funding acquisition, Methodology. All authors have given approval to the final version of the manuscript.

Conflicts of interest

The authors declare no conflict of interest.

Acknowledgements

This study was supported in part by a Grant-in-Aid for JSPS Fellow (JP21J10674) and Program for Leading Graduate Schools "Ambitious Leader's Program (ALP)" at Hokkaido University. Part of this study was conducted at the Multi-Quantum Beam High Voltage Electron Microscope Laboratory at Hokkaido University, supported by the Nanotechnology Platform Program of the Ministry of Education, Culture, Sports, Science and Technology (MEXT), Japan (A-19-HK-0003, A-20-HK-0002, A-21-HK-0035). DK would like to acknowledge financial support from the National Science Center (NCN), Poland (grant number 2020/39/B/ST4/02548). We thank Prof. Norihito Sakaguchi and Mr. Ryo Ota (Faculty of Engineering, Hokkaido University) for their technical assistance and helpful discussions on STEM/EELS analysis. Mr. Seongwoo Jeong and Mr. Ruijie Zhu(Graduate School of Chemical Sciences and Engineering, Hokkaido University) are acknowledged for their technical help and suggestion about the DFT calculations. YS thanks Mr. Takuya Shimajiri (Graduate School of Chemical Sciences and Engineering, Hokkaido University) for his fruitful comments regarding the carbon atom electronic state.

Notes and references

1 T. Hasegawa, S.R. Mukai, Y. Shirato, and H. Tamon, *Carbon*, 2004, **42**, 2573-2579.
2 H. Habazaki, M. Kiriu, and H. Konno, *Electrochem. Commun.*, 2006, **8**, 1275-1279.
3 Y. Zhai, Y. Dou, D. Zhao, P.F. Fulvio, R.T. Mayes, and S. Dai, *Adv. Mater.,* 2011, **23**, 4828-4850.
4 J. Ou, L. Yang, and X. Xi, *Chinese J. Chem.*, 2016, **34**, 727-732.
5 B. Li, J. Zheng, H. Zhang, L. Jin, D. Yang, H. Lv, C. Shen, A. Shellikeri, Y. Zheng, R. Gong, J.P. Zheng, and C. Zhang, *Adv. Mater.,* 2018, **30**, 1705670.
6 M. Takeno, S. Katakura, K. Miyazaki, T. Abe, and T. Fukutsuka, *Electrochemistry (Tokyo)*, 2021, **89**, 585-589.
7 M. Kiriu, K. Fushimi, H. Konno, and H. Habazaki, *Electrochemistry (Tokyo)*, 2008, **76**, 197-202.
8 S.K. Ahn, J.J. Yanf, H. Kim, H. Habazaki, and S.G. Park, *Chem. Lett.,* 2014, **43**, 898-900.
9 B. Li, F. Dai, Q. Xiao, L. Yang, J. Shen, C. Zhang, and M. Cai, *Adv. Energy Mater.,* 2016, **6**, 1600802.
10 P. Han, G. Xu, X. Han, J. Zhao, X. Zhou, and G. Cui, *Adv. Energy Mater.,* 2018, **8**, 1801243.
11 C. Zhu, M. Takata, Y. Aoki, and H. Habazaki, *Chem. Eng. J.*, 2018, **350**, 278-289.
12 W. Fu, E. Zhao, R. Ma, Z. Sun, Y. Yang, M. Sevilla, A.B. Fuertes, A. Magasinski, and G. Yushin, *Adv. Energy Mater.,* 2019, **10**, 1902993.
13 C. Kim, C. Zhu, Y. Aoki, and H. Habazaki, *Electrochim. Acta*, 2019, **314**, 173-187.
14 P. Li, D. Zhang, Y. Xu, C. Ni, G. Shi, and X. Sang, *Chin. J. Chem. Eng.*, 2019, **27**, 709-716.
15 J. Cao, H. Xu, J. Zhong, X. Li, S. Li, Y. Wang, M. Zhang, H. Deng, Y. Wang, C. Cui, M. Hossain, Y. Cheng, L. Fan, L. Wang, T. Wang, J. Zhu, and B. Lu, *ACS Appl. Mater. Interfaces*, 2021, **13**, 8497–8506.
16 Z. Siroma, K. Ishii, K. Yasuda, Y. Miyazaki, M. Inaba, and A. Tasaka, *Electrochem. Commun.,* 2005**, 7,** 1153-1156.
17 T. Kinumoto, K. Takai, Y. Iriyama, T. Abe, M. Inaba, and Z. Ogumi, *J. Electrochem. Soc.,* 2006**, 153,** A58-A63.
18 E. Tsuji, T. Yamasaki, Y. Aoki, S.G. Park, K. Shimizu, and H. Habazaki, *Carbon*, 2015, **87,** 1-9.
19 L. Castanheira, W.O. Silva, Fabio H.B. Lima, A. Crisci, L. Dubau, and F. Maillard, *ACS Catal.,* 2015, **5**, 2184–2194.
20 P. J. Kulesza, J. K. Zak, I. A. Rutkowska, B. Dembinska, S. Zoladek, K. Miecznikowski, E. Negro, V. D. Noto, and P. Zelenay, *Curr. Opin. Electrochem.*, 2018, **9,** 257-264.
21 N. Yamada, D. Kowalski, C. Zhu, Y. Aoki, and H. Habazaki, *RSC Adv.*, 2019, **9,** 3726-3733.
22 T. Kang, J. Lee, J.G. Kim, and C. Pak, *J. Electrochem. Sci. Technol.*, 2021, **12,** 137-147.
23 K. Wang, N. Li, Y. Yang, S. Ke, Z. Zhang, M. Dou, and F. Wang, *Chin. Chem. Lett.*, 2021, **32**, 3159-3163.
24 R. Mohamed, X. Cheng, E. Fabbri, P. Levecque, R. Kotz, O. Conrad, and T. J. Schmidt, *ECS Trans.*, 2014, **58,** 9-18.
25 Y. Zhu, W. Zhou, and Z. Shao, *Small*, 2017, *13(12)*, 1603793.
26 Y.J. Min, S.J. Oh, M.S. Kim, J.H. Choi, and S. Eom, *J. Appl. Electrochem.,* 2018, **48,** 405-413.
27 C. Alegre, C. Busacca, A.D. Blasi, O.D. Blasi, A.S. Aricò, V. Antonucci, E. Modica, and V. Baglio, *J. Energy Storage,* 2019*,* **23,** 269-277.
28 C. Alegre, C. Busacca, A.D. Blasi, O.D. Blasi, A.S. Aricò, V. Antonucci, and V. Baglio, *ChemElectroChem*, 2020, **7,** 24-30.
29 Y. Sato, D. Kowalski, Y. Aoki, and H. Habazaki, *Appl. Cat. A: General*, 2020, **597,** 117555.
30 Y. Sato, S. Kitano, D. Kowalski, Y. Aoki, N. Fujiwara, T. Ioroi, and H. Habazaki, *Electrochemistry (Tokyo).*, 2020, **88,** 566-573.
31 Y. Sugawara, T. Hihara, G.M. Anilkumar, K. Kamata, and T. Yamaguchi, *Sustainable Energy & Fuels*, 2021, **5,** 1374-1378.
32 M. Pourbaix, Atlas of Electrochemical Equilibria in Aqueous Solutions, Pergamon Press Ltd., United Kingdom, 1966, pp 449-457.
33 K. Kinoshita, Carbon: Electrochemical and Physicochemical Properties, John Wiley & Sons, United States of America, 1988, pp 334.
34 M. Tominaga, Y. Yatsugi, and N. Watanabe, *RSC Adv.*, 2014, **4,** 27224-27227.
35 K. Ono, T. Kinumoto, T. Tsumura, and M. Toyoda, *ECS Trans.*, 2015**, 64,** 29-39.
36 W. Lee, J. Park, J. Park, S.J. Kang, Y. Choi, and Y. Kim, *J. Mater. Chem. A*, 2020,**8**, 9185-9193
37 S.G. Ji, H. Kim, W.H. Lee, H.S. Oh, and C.H. Choi, *J. Mater. Chem. A*, 2021, **9**, 19834-19839.
38 W. Xu, D. Cao, O.A. Moses, B. Sheng, C. Wu, H. Shou, X. Wu, S. Chen, and L. Song, *Nano Res.*, 2021, DOI: 10.1007/s12274-021-3368-1.
39 T. Fujigaya, S. Hirata, M.R. Berber, and N. Nakashima, *ACS Appl. Mater. Interfaces*, 2016, **8,** 14494-14502.
40 T. Fujigaya, Y. Shi, J. Yang, H. Li, K. Ito, and N. Nakashima, *J. Mater. Chem. A*, 2017, **5,** 10584-10590.
41 J. Yang, T. Fujigaya, and N. Nakashima, *Sci. Rep.*, 2017, **7**, 45384.
42 P. Ross and M. Sattler, *J. Electrochem. Soc.*, 1988, **135,** 1464-1470.
43 C.C. Hung, P.Y. Lim, J.R. Chen, and H.C. Shih, *J. Pow. Sou.*, 2011, **196,** 140-146.
44 Y.P. Hsieh, M. Hofmann, K.W. Chang, J.G. Jhu, Y.Y. Li, K.Y. Chen, C.C. Yang, W.S. Chang, and L.C. Chen, *ACS Nano,* 2014, **8,** 443-448.
45 H. Nishihara, T. Simura, S. Kobayashi, K. Nomura, R. Berenguer, M. Ito, M. Uchihara, H. Iden, K. Arihara, A. Ohma, Y. Hayasaka, and T. Kyotani, *Adv. Funct. Mater.*, 2016, **26,** 6148-6427.
46 S.P. Rodríguez, D. Sebastián, and M.J. Lázaro, *Electrochimica Acta*, 2019, **303,** 167-175.
47 L. Tao, Q. Wang, S. Dou, Z. Ma, J. Huo, S. Wang, and L. Dai, *Chem. Commun.*, 2016, **52,** 2764–2767.

48 N. Staud, H. Sokol, and P.N. Ross, *J. Electrochem. Soc.*, 1989, **136,** 3570-3576.
49 M. Matsumoto, T. Manako, and H. Imai, *J. Electrochem. Soc.*, 2009, **156,** B1208-1211.
50 G.F. Han, B.B. Xiao, S.J. Kim, F. Li, I. Ahmad, I.Y. Jeon, and J.B. Baek, *Nano Energy,* 2019**, 66,** 104112.
51 R. Tang, K. Taguchi, H. Nishihara, T. Ishii, E. Morallon, D. Cazorla-Amoros, T. Asada, N. Kobayashi, Y. Muramatsu, and T. Kyotani, *J. Mater. Chem. A,* 2019, **7,** 7480-7488.
52 H. Habazaki, M. Kiriu, M. Hayashi, and H. Konno, *Mater. Chem. Phys.*, 2007, **105,** 367-372.
53 S. Lim, S. H. Yoon, and I. Mochida, J. H. Chi, *J. Phys. Chem. B*, 2004, **108,** 1533-1536.
54 T. Tamaki, H. Wang, N. Oka, I. Honma, S.H. Yoon, and T. Yamaguchi, *Int. J. Hydrogen Energy*, 2018, **43,** 6406-6412.
55 S.W. Lee, S.R. Choi, J. Jang, G.G. Park, S.H. Yu, and J.Y. Park, *J. Mater. Chem. A*, 2019, **7,** 25056-25065.
56 S.G. Peera, R. Koutavarapu, S. Akula, A. Asokan, P. Moni, M. Selvaraj, J. Balamurugan, S.O. Kim, C. Liu, and A.K. Sahu, *Energy Fuels*, 2021, **35,** 11761-11799.
57 N. Hodnik, G. Dehm, and K.J.J. Mayrhofer, *Acc. Chem. Res.*, 2016, **49,** 2015−2022.
58 N. Hodnik, M. Zorko, M. Bele, S. Hočevar, and M. Gaberšček, *J. Phys. Chem. C*, 2012, **116,** 21326–21333.
59 T. Kinumoto, H. Nishihara, M. Matsuoka, N. Eguchi, T. Tsumura, and M. Toyoda, *Electrochemistry (Tokyo)*, 2015, **83,** 12-17.
60 A. Ooi, Y. Shigihara, E. Tada, and A. Nishikata, *Materials Transactions*, 2020, **61,** 1949-1957.
61 Y. Hou, N. Kovács, H. Xu, C. Sun, R. Erni, M.J. Gálvez-Vázquez, A. Rieder, H. Hu, Y. Kong, M. Liu, B.J. Wiley, S. Vesztergom, and P. Broekmann, *J. Catal.*, 2021, **394,** 58-66.
62 N. P. Finkelstein, and R. D. Hancock, *Gold Bulletin*, 1974, **7,** 72-77.
63 K. Nishio, and H. Masuda, *Angew. Chem. Int. Ed.,* 2011, **50,** 1603-1607.
64 K. Nishio, and H. Masuda, *Bull. Chem. Soc. Jpn.*, 2013, **86,** 1144-1150.
65 K. Sakai, Y. Kitazumi, O. Shirai, and K. Kano, *Anal. Sci.,* 2018, **34,** 1317-1322.
66 H. Konno, K. Oyamada, and M. Inagaki, *J. Euro. Ceramic Soc.*, 2000, **20,** 1391-1396.
67 H.H. Elsentriecy, and K. Azumi, *J. Electrochem. Soc.*, 2009, **156,** D70-D77.
68 Y. Konno, E. Tsuji, Y. Aoki, T. Otsuka, and H. Habazaki, *Faraday Discussions*, 2015, **180,** 479-493.
69 K.A. Mkhoyan, A.W. Contryman, J. Silcox, D.A. Stewart, G. Eda, C. Mattevi, S. Miller, and M. Chhowalla, *Nano Lett.*, 2009, **9,** 1058–1063.
70 K. Miyazawa, T. Nagai, K. Kimoto, M. Yoshitake, and Y. Tanaka, *Surf. Interface Anal.*, 2021, **53,** 84-89.
71 K. Miyazawa, T. Nagai, K. Kimoto, M. Yoshitake, and Y. Tanaka, *Surf. Interface Anal.*, 2020, **52,** 23-33.
72 D.D' Angelo, C. Bongiorno, M. Amato, I. Deretzis, A. La Magna, G. Compagnini, S.F. Spanò, and S. Scalese, *Carbon*, 2015, **93,** 1034-1041.
73 M. Pelaez-Fernandez, A. Bermejo, A.M. Benito, W.K. Maser, and R. Arenal, *Carbon,* 2021**, 178,** 477-487.
74 A. Braun, F.E. Huggins, N. Shah, Y. Chen, S. Wirick, S.B. Mun, C. Jacobsen, and G.P. Huffman, *Carbon,* 2005**, 43,** 117-124.
75 Y. Lin, Q. Lu, F. Song, L. Yu, A.K. Mechler, R. Schlögl, and S. Heumann, *Angew. Chem. Int. Ed.,* 2019**, 58,** 8917-8921.
76 S. Möller, S. Barwe, J. Masa, D. Wintrich,S. Seisel, H. Baltruscha, and W. Schuhmann, *Angew. Chem. Int. Ed.,* 2020**, 59,** 1585-1589.
77 A. Ikezawa, K. Miyazaki, T. Fukutsuka, and T. Abe, *Electrochemistry (Tokyo)*, 2022, **90**, 017011.